Plasma probe characteristics in low density hydrogen pulsed plasmas

2015 Plasma Sources Sci. Technol. 24 055018

(http://iopscience.iop.org/0963-0252/24/5/055018)

IOP Publishing Plasma Sources Science and Technology

Plasma Sources Sci. Technol. **24** (2015) 055018 (10pp) doi:10.1088/0963-0252/24/5/055018

Plasma probe characteristics in low density hydrogen pulsed plasmas

D I Astakhov[1,6], W J Goedheer[2], C J Lee[1], V V Ivanov[3], V M Krivtsun[3], A I Zotovich[4,5], S M Zyryanov[5], D V Lopaev[5] and F Bijkerk[1]

[1] XUV Group, MESA + Institute for Nanotechnology, University of Twente, PO Box 217, 7500 AE Enschede, The Netherlands
[2] FOM Institute DIFFER—Dutch Institute for Fundamental Energy Research, PO Box 1207, 3430 BE Nieuwegein, The Netherlands
[3] Institute for Spectroscopy RAS (ISAN), Fizicheskaya 5, Troitsk 142190, Russian
[4] Faculty of Physics, Lomonosov Moscow State University, Leninskie Gory, Moscow 119991, Russian
[5] Skobeltsyn Institute of Nuclear Physics, Lomonosov Moscow State University, Leninskie Gory, Moscow 119991, Russian

E-mail: d.i.astakhov@gmail.com

Received 10 December 2014, revised 19 June 2015
Accepted for publication 14 August 2015
Published 15 September 2015

Abstract

Probe theories are only applicable in the regime where the probe's perturbation of the plasma can be neglected. However, it is not always possible to know, *a priori*, that a particular probe theory can be successfully applied, especially in low density plasmas. This is especially difficult in the case of transient, low density plasmas. Here, we applied probe diagnostics in combination with a 2D particle-in-cell model, to an experiment with a pulsed low density hydrogen plasma. The calculations took into account the full chamber geometry, including the plasma probe as an electrode in the chamber. It was found that the simulations reproduce the time evolution of the probe IV characteristics with good accuracy. The disagreement between the simulated and probe measured plasma density is attributed to the limited applicability of probe theory to measurements of low density pulsed plasmas on a similarly short time scale as investigated here. Indeed, in the case studied here, probe measurements would lead to, either a large overestimate, or underestimate of the plasma density, depending on the chosen probe theory. In contrast, the simulations of the plasma evolution and the probe characteristics do not suffer from such strict applicability limits. These studies show that probe theory cannot be justified through probe measurements. However, limiting cases of probe theories can be used to estimate upper and lower bounds on plasma densities. These theories include and neglect orbital motion, respectively, with different collisional terms leading to intermediate estimates.

Keywords: pulsed plasma, particle-in-cell, probe theory, hydrogen plasma, low pressure, low density plasma

(Some figures may appear in colour only in the online journal)

I. Introduction

Low pressure (1..100 Pa) low density ($n_e \sim 10^8..10^9$ cm^{-3}) pulsed plasmas are commonly found in many laboratory experiments. These plasmas can exhibit complicated behavior because they can be operated in the non-local and non-stationary regime.

However, in practice, plasmas of this type are frequently investigated with the Langmuir probe technique. But the application of plasma probe diagnostics is hindered, because it strictly requires [1, 2] (a) that the plasma is distorted by the probe only locally in a well defined manner, and (b) that the evolution of the plasma, excluding the distorted region, is not affected by the presence of the probe.

[6] Author to whom any correspondence should be addressed.

Probe diagnostics were initially designed for glow discharge plasmas, where the applicability limits could be estimated in advance easily. Thus, Langmuir probe measurements allowed plasma parameters, such as the electron density and temperature, to be derived with the help of appropriate formulas. However, the probe method does not provide a technique to estimate the applicability of the method itself.

Nevertheless, in many experiments with a lower density plasma there is not enough information to justify the probe method beforehand. Thus, the plasma parameters, which are obtained from probe measurements with help of probe theory, are used to evaluate the methods applicability.

Applying a probe theory outside of its applicability limits leads to errors in the plasma parameters derived from the measured probe response. Frequently, in day to day practice, the probe method validity is estimated from two observations: (a) the probe I–V characteristic should have distinct ion and electron contributions, and (b) the plasma size should be at least a factor of 100 larger than the estimated Debye length [2]. However, these parameters, derived from the probe measurements, have a tendency to support the validity of the probe method, e.g. if the derived electron density is overestimated for a low density plasma (see section IV.D for example and discussion), the second condition is satisfied in most cases.

In order to overcome these difficulties, we propose to use a combined approach, where experiments and simulations are coupled as tightly as possible, with the full experimental geometry included in simulations. In these simulations, the plasma probe is included as an additional electrode. By including the probe in the model, any effect that it has on the plasma is naturally included in the dynamics. This approach does not have any of the restrictions discussed above.

In general this requires a 3D plasma model. Such simulations are extremely time consuming, but, fortunately, it is possible to reduce the model dimensions by using of an axis-symmetrical configuration for the experimental setup. This allows a 2D cylindrically symmetric model to be used for the plasma simulation, which is much faster than a 3D model.

In this paper, we show that, especially in the case where the spatial homogeneity of the plasma cannot be easily verified, one needs to be very careful interpreting the results from probes. We consider a discharge that produces probe characteristics with the proper response. Using several probe theories (see below), we show that they all self consistently report densities, temperatures, and dimensions that would lead one to conclude that the probe theory is correct. However, not only are these theories mutually inconsistent, a 2D PIC model of the same plasma shows that the probe theories are highly likely to be inconsistent with the experimental plasma densities as well. The difference between the PIC model and the probe theories was attributed to the distortion of the plasma by the probe, and to transient plasma dynamics.

II. Experimental setup

The interior configuration of the vacuum chamber, in which the low density H_2 pulsed plasma was generated, is presented in figure 1. The chamber was pumped with a turbomolecular pump to keep the residual gas pressure lower than 0.003 Pa. During experiments, hydrogen flowed through the chamber at several sccm, controlled by a gas flow meter. The hydrogen pressure in the chamber was varied in the range of 0–60 Pa.

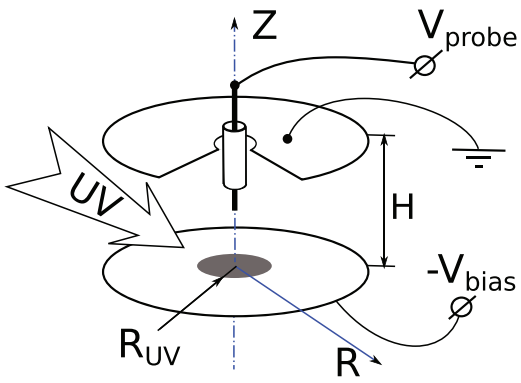

Figure 1. Configuration of the experimental chamber. The electrodes are 10 cm in diameter and separated by 5 cm. The plasma probe passes through the center of the top electrode and is 3 cm from the bottom electrode. The open end of the probe is 1 cm in length and 0.5 mm in diameter. The remainder of the probe is covered by a dielectric with a length of 1 cm and a diameter of 1.3 mm. The plate holders and chamber walls are not show, because the vacuum chamber is large (cylinder 20 cm in diameter and 20 cm in height).

The aluminum electrodes are circular plates with a 10 cm diameter. The distance between the electrodes can be varied in the range of 2–5 cm. In the experiments, the bottom electrode was negatively biased at −200 to 0 V, while the top electrode was grounded. The bias was kept at a constant value during the plasma ignition and decay. The plasma was ignited by the photoelectrons emitted from the bottom electrode during the UV laser pulse. Most of these electrons are reflected back to the bottom electrode by the space charge field. The electrons which pass the potential barrier, are accelerated by the applied bias field and ionize the background gas, thus igniting the plasma.

A KrF excimer laser (LPX210) was used as the source of the UV radiation that produces photoelectrons at the bottom electrode. The temporal profile of the laser pulse consists of a short pulse with a full width half maximum (FWHM) of $<$50 ns and a tail, extending up to 200–300 ns in duration (see figure 2). The pulse energy, incident on the bottom electrode, was approximately 10 mJ/pulse, which was only 20% of total laser pulse energy. Approximately the same fraction of the total laser energy was reflected to a detector by a beam splitter to control the laser pulse energy during the experiment. The laser beam was passed through a diaphragm to obtain a uniform intensity distribution with a diameter of 1.3 cm at the bottom electrode. The laser light was incident at an angle to the electrode after entering the chamber through a quartz window.

The plasma probe was installed along the symmetry axis of the chamber. The probe was 0.05 cm in diameter and 1 cm long, the glass shield that covers the rest of the probe was 0.13 cm in diameter. The probe measurements were automated with a NI-DAQ card and specially developed signal processing unit (SPU), consisting of a trans-impedance isolated amplifier, differential amplifier, and probe bias control. This unit allows probe currents down to 10 nA to be measured

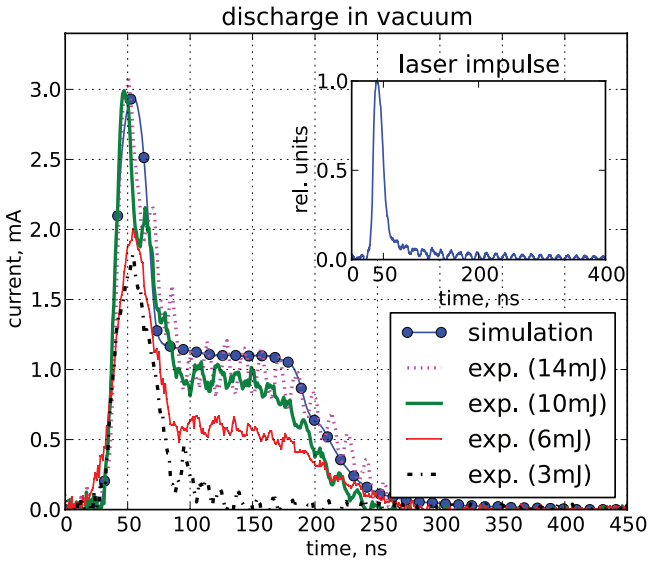

Figure 2. Discharge current in vacuum conditions, −200 V bias. Laser pulse temporal profile for 10 mJ/pulse (inset). The current due to the main laser pulse is in the saturation regime. The difference between 6 mJ/pulse and 10 mJ/pulse peak currents can be attributed to some higher order effects, since the peak values for 3 mJ/pulse and 6 mJ/pulse are very close. Step-like current tail is due to laser tail. The current tails for 10 mJ/pulse and 14 mJ/pulse are very close in magnitude, justifying the choice of 10 mJ/pulse as the energy for experiments. The simulation data correspond to the fine tuned laser pulse shape (see text) for 10 mJ/pulse. The temporal pulse shape of the laser, as measured by the detector is presented in the insert.

in the band of approximately 6 MHz. The signals amplified by the SPU were transferred to an oscilloscope (Tektronix TDS3032). The overall control of measurements and the experimental setup was performed with a computer program via the NI-DAQ card, as well as GPIB, and RS232 interfaces. The obtained data were stored on a server for further analysis.

III. Model

The plasma was modelled using a two-dimensional (*rz* cylindrically symmetric) particle-in-cell (PIC) model. The plasma species include electrons, H^+, H_2^+ and H_3^+ as particles for accurate description of processes in the plasma sheath. Our model follows the general PIC scheme, described elsewhere [3].

The combination of measurements and simulations of discharge characteristics and plasma probe measurements allows the number of free parameters to be reduced. These parameters (e.g. ion induced electron emission yield, photo electron yield, initial electron energy distribution etc) are required to perform simulations, but the range of values found in literature are typically too large for accurate modeling. It is worth noting here that many such parameters are intrinsically setup dependent (i.e. the photo electron yield could be very sensitive to the surface conditions). Thus, preferably, such parameters should be measured.

An accurate measurement of all unknown parameters is often unfeasible. To solve this issue, the model was developed in parallel to the experimental setup. Thus, many of the unknown parameters were obtained with reasonable accuracy using the results from simple experiments, which were performed as a test procedure during the construction and calibration of the experiment.

III.A. UV laser and electron spectrum used as input to the model

In the experiment, an excimer laser, operating at a wavelength of 248 nm, generates photoelectrons from the bottom electrode. In the model, this process is included as a photoelectron source on the bottom electrode. On each time step, when the laser is active, photoelectrons are released from the irradiated part of the bottom electrode to the computational domain. The amount of injected electrons is linearly proportional to the instantaneous laser intensity. The electron energies are sampled according to a distribution, as discussed below. The velocities of the injected electrons are distributed according to a cosine law relative to the normal direction to the boundary.

The initial electron energy distribution and the temporal profile of the laser pulse are important parameters that significantly influence the plasma that is formed later. Under vacuum conditions, where no plasma is ignited, the temporal profile of the current contains information about the laser pulse shape and the effective photoelectron yield. We used this experiment and the following physically motivated choice of parameters to define the effective electron source for the model.

The laser energy per pulse in the experiment was 10 mJ. The typical photoelectron emission yield is estimated to be 10^{-4}–10^{-3} electrons/photon [4], thus, the maximum collected charge is approximately 20–200 nC. However, in the experiment, the collected charge per pulse under vacuum conditions was approximately 0.2 nC. Hence, the space charge current limiting was very high during the main part of the laser pulse.

The space charge potential barrier formation leads to a locally high electron density. The electrons, which are trapped by the barrier, have small energies, thus, Coulomb collision processes should dominate. From a computational point of view it is not reasonable to compute the full collision kinetics of the cold electrons, since it is known to lead to the formation of a Maxwellian tail in the energy distribution, and the detailed kinetics depend on the exact initial distribution and photoelectron yield, which are not known. Thus, a Maxwellian function was taken as the initial electron energy distribution function (EEDF).

The effective temperature for this EEDF was heuristically chosen from two observations. Firstly, the bottom electrode was made from aluminum, which might by partially oxidized. A number of values for the work function of this material have been reported, the lowest of which is about 4 eV [5]. Secondly, since the photoelectron yield is not known precisely, we only need to find a reasonable combination of effective temperature and yield to reproduce the charge-bias characteristic, as measured experimentally under vacuum conditions. Thus, the effective temperature for EEDF was chosen to be 0.5 eV, and the value for photoelectron yield was fine-tuned from the measured vacuum charge bias characteristics of the system. Because of the significant space charge screening, the sensitivity for the particular choice is small.

A scan over laser pulse energies from 3 mJ to 15 mJ was performed to ensure that the experiment was stable. It was found that the vacuum discharge characteristics have the lowest sensitivity to the laser power variation near 10 mJ/pulse. However, while the integral value was stable, there were signs of higher order processes (e.g. two photon photoelectric effect), since the value of the vacuum current peak changed near a laser pulse energy of 6 mJ (see figure 2). These experiments were included into the fitting procedure, and it was found that while for all energies below 6 mJ/pulse the above described procedure produced consistent results, it was not possible to reproduce the current peak value for 10 mJ/pulse and above due to space charge screening. For this reason, a very small amount of 4 eV electrons, with a yield of approximately 10^{-8}, was added to the electron source to describe the case of 10 mJ/pulse laser energy.

As mentioned above, the laser pulse shape has a tail (up to 300 ns) in comparison to the 60 ns main pulse (see figure 2). This tail plays a very important role in plasma formation as discussed in section IV.A. Unfortunately, the radiation intensity in the laser tail was too low to accurately measure with our equipment. This fact also suggests that one should not expect a space charge effect. For this reason, the EEDF for the electrons generated by the tail of the pulse is constant for all electron energies less than 1 eV, and zero for higher energies.

A fitting procedure was used to derive the laser tail shape from the measured discharge characteristics in vacuum. During this procedure the pulse shape was represented as the sum of the measured laser pulse and a tail. The electron yield was chosen such that it reproduced the peak current value and the tail current simultaneously.

III.B. Ion induced electron emission

It is important to take into account ion induced electron emission, since free electrons are accelerated by the electric field to the top electrode and produce additional electrons and ions through impact ionization. The electrons produced through impact ionization contribute significantly to the later dynamics of the plasma and should be taken into account.

The bottom electrode in the experiment was biased at −200 to 0 V, therefore, the maximum ion energy is about 200 eV. For this energy range, the ion induced electron emission can be represented as a sum of potential emission (PE) and kinetic-induced emission (KE) [6, 7]. The PE yield is determined by the combination of the ion and target material, however, for the slow ions it is independent of the ion velocity. But, the KE yield (see below) strongly depends on the ion velocity.

In the model, the PE probability to emit an electron per one ion impact at the bottom electrode is computed with the following semi-empirical formula from [8]

$$\gamma \approx \frac{0.2}{E_F}(0.8E_i - 2W) \qquad (1)$$

Here E_F is the metal Fermi energy, E_i is *ionization* energy of the ion and W is the metal's work function. The applicability range of equation (1) is $3W \leqslant E_i \leqslant (2E_F + W)$, the accuracy of this approximation in these range is not better than 10%. Outside this range, the accuracy of equation (1) slowly decreases.

The top and bottom electrodes (see figure 1) are made from aluminum. The tabulated values for aluminum are $E_F = 11.7$ eV, $W = 3.8$–4.5 eV. The large spread in work function can be attributed to a combination of the effect of the surface crystalline structure [5] and of surface oxide, which can lead either to an increase or a decrease of the observed work function, depending on the exact conditions [9]. The plasma probe is made from molybdenum, which has a Fermi energy and work function of $E_F = 6.8$ eV, $W = 4.2$–4.6 eV [5, 10].

For a hydrogen plasma there are three types of ions possible. The ions have ionization energies of: H^+ 13.6 eV, H_2^+ 15.4 eV, and H_3^+ 3.6 eV. The value used for H_3^+ here is the ionization potential for a long lived H_3 taken from [11]. This definition of H_3^+ ionization energy is less than twice the energy of the work functions of aluminum or molybdenum, thus, H_3^+ does not produce any potential emission. Hence, the PE probability for H^+ is approximately 0.04 ± 0.02 on aluminum and 0.06 ± 0.02 on molybdenum, while for H_2^+—0.07 ± 0.02 on aluminum and 0.1 ± 0.02 on molybdenum. In these estimates we included an error of at least 10% due to the approximation used and further 10% error due to the poor knowledge of work function.

There are complicated KE models [12], but they require some fitting parameters to be defined. Since the exact surface conditions are not known well, the same accuracy is obtained by simply fitting to experimental data [7]. Therefore, we follow the same approach as in [13], and use a fit to the experimental data [7] to determine for KE for all metallic surfaces.

$$\gamma_{KE} \approx 6.2 \cdot 10^{-5} \cdot (E[\text{eV amu}^{-1}])^{1.15} \qquad (2)$$

Here E is the *kinetic* energy of the ion per ion mass.

The physical motivation for this approach is as follows. For many metals and conductive materials, the work function (W) is approximately 5 eV and the quasi-classical threshold of KE is $v_i > W/(2k_F)$, here v_i is the ion velocity and k_F is a Fermi impulse. KE depends strongly on the ion type and target material, especially for heavy ions. But, in experiments [7], the KE probability, as a function of velocity, varies only by a factor of two or less for H^+, H_2^+ and H_3^+ (for a gold target). Similar experiments indicate that, for a given ion species, KE is similar for a broader range of target materials [14].

In our simulation, the use of an ion-type-dependent ion-induced electron emission coefficient leads to time-dependent ion-induced emission, because, just after the UV pulse, the main ion is H_2^+ and the ion induced emission coefficient is large. However, due to a very efficient ion conversion reaction $H_2^+ + H_2 \rightarrow H_3^+ + H$, the role of ion-induced emission significantly decreases after a characteristic ion conversion time.

Although the approximations for PE and KE are rather simple, they provide reasonable estimates of ion-induced emission. For instance, this simple model allows us to distinguish between a discharge initiated by a laser pulse without a tail and a large ion-induced emission coefficient, and the case

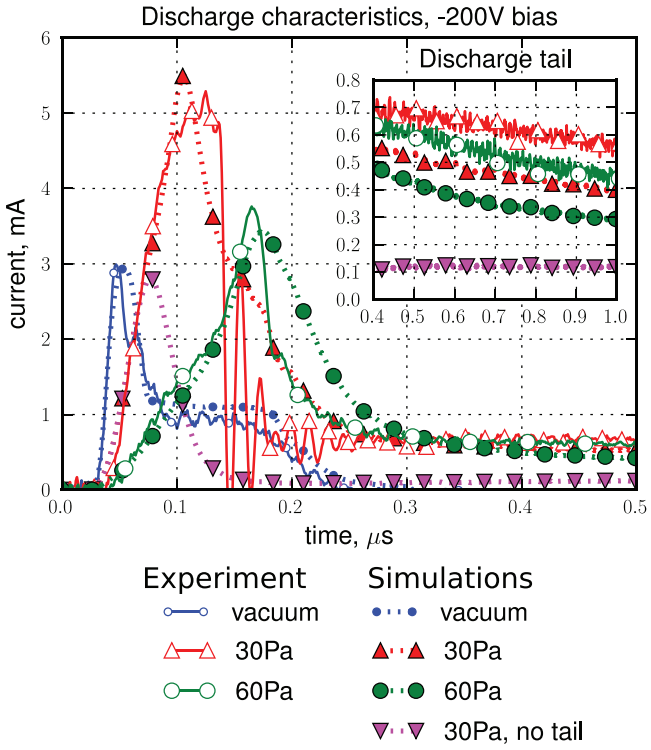

Figure 3. Discharge current as function of time for various hydrogen pressures. The tail of discharge is shown in inset in the same units as main plot. Note, that the laser pulse tail (see figure 2) produces a significant contribution to plasma formation, as suggested by comparison of simulation results for 30 Pa with and without laser pulse tail.

with a smaller ion-induced emission coefficient and a laser pulse with a tail (as in figure 3).

III.C. Length scales, grid resolution

The spatial resolution of the rectilinear grid is chosen to resolve two main characteristic length scales: the space charge potential well and the Debye length. The space charge potential well length scale can be estimated from the analytical solution for a 1D diode with a Maxwellian initial electron energy distribution [15]. In the considered case, most photoelectrons are reflected back to the surface. Thus, it is possible to simplify the formulas from [15] and obtain

$$z_m \simeq 0.1 \text{ cm} \times \frac{(T[\text{eV}])^{3/4}}{(I[\text{mA cm}^{-2}])^{1/2}} \qquad (3)$$

Here, T is the initial temperature of emitted photoelectrons, I is the current density near the cathode and z_m is the distance from the cathode and the bottom of the space charge potential well. For $T \sim 0.5$ eV and $I \sim 2$ mA cm^{-2}, one obtains $z_m \sim 0.04$ cm. Since the UV spot diameter is much larger than the estimated z_m, the z_m length scale should only be resolved in the z direction near the bottom electrode. For the plasma region, the grid cell size is estimated as the Debye radius, r_D, for a plasma with $n_e \sim 10^9$ cm^{-3}, and $T_e \sim 0.5$ eV, which corresponds to $r_D \sim 0.02$ cm. We ran several tests to ensure that the grid resolution does not affect our results.

The displacement currents to the probe and electrodes are also included in the model. They are computed at each time step as the numerical derivative of the electric field over each of the electrode boundaries. Inclusion of the displacement current allows direct comparison between the simulated and experimental discharge currents.

To calculate the production of the different ion species, a set of the cross-sections for the hydrogen chemistry was assembled from the several sources. The data from [16] was used as a base, and extended using the work of [17, 18].

The procedure described in [19] is used to perform Monte Carlo collisions with the background gas. This procedure allows a reaction channel to be chosen before sampling the reaction probability, which offers significant performance improvement compared to the Null collision scheme [20].

We neglect the formation of H^-. The cross-section of dissociative electron attachment is significant only if H_2 is high vibrationally excited (e.g. $v = 4$) [21]. However, the density of H_2 molecules in these states is expected to be very low, since the corresponding cross-sections of the direct excitations are small [22]. The stepwise excitations are expected to give negligible contribution due to small ratio of the concentrations of vibrationally excited H_2 and H_2 in the ground state.

We tested the consistency of our implementation by modeling swarm experiments and found good agreement with experimental values [23] for electron ionization coefficients, electron mobility and for H^+, H_3^+ mobility in hydrogen [24].

IV. Results and discussion

IV.A. Discharge characteristics

Let us begin with the analysis of the discharge characteristics of the experimental setup without a plasma probe.

During the laser pulse, only a small amount of photoelectrons enter the chamber because of the space-charge-induced potential barrier. This barrier is not just due to the electron cloud trapped near the bottom electrode, but is built up by all the excess negative charge present in the chamber. Hence, simulations under vacuum conditions (i.e. no plasma) provide a good estimate of the temporal profile of the laser pulse, but they are not very sensitive to the magnitude of electron emission. In the model, the temporal profile of the laser pulse was fine-tuned such that it reproduced the current maximum for the case of 30 Pa, −200 V bias. This was sufficient to yield good agreement with experimental data for the maximum current under all other considered conditions.

The current as function of time for −200 V bias at different background pressures is presented in figure 3. The laser pulse tail (see figure 2) produces a significant contribution to the plasma formation (see comparison of cases with and without tail in figure 3). This happens because the electrons produced during the body of the laser pulse provide ionization in the chamber, which leads to the formation of the plasma. The presence of this plasma changes the potential distribution inside the chamber, leading to an increased field strength near the bottom electrode, which, in turn, increases the efficiency of ionization, thus, enhancing the effect of the laser pulse tail.

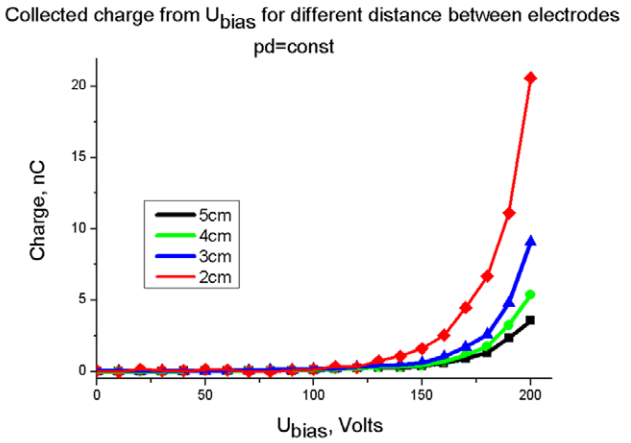

Figure 4. Collected charge for different distances between electrodes, but constant pd (for $d = 5$ cm, $p = 30$ Pa).

Despite reproducing both the slope of the current increase, and the current maximums for both pressures, the magnitude of the simulated discharge tail is about 30% lower than in the experiment. Agreement between our simulations of the discharge tail, and the experimental data can be obtained by varying the tail of the laser pulse. Under these conditions, however, the peak position and width of the current were significantly distorted at pressures of 30 Pa and 60 Pa. Alternatively, increasing PE and KE also yields a discharge tail in agreement with experimental data. This, however, results in unrealistically high ion induced electron emission yield for H_3^+ ion (e.g. ~0.05 electron/ion on average). Moreover, the model fails to reproduce the Langmuir probe measurements in this case.

Therefore, the disagreement between the model and experimental data is probably due to an accumulation of minor differences between the input parameters of the model and the experiment. These could be, for example, the laser spot size, uncertainties in the cross-sections set, pulse-to-pulse variations of laser pulse tail, etc. Nevertheless, the 30% difference between the plasma model and the experimental data is reasonably accurate for the probe simulations.

IV.B. Plasma scalability

Additional experiments were performed to study the plasma scalability for different distances between electrodes, with fixed pd parameter (here is p—hydrogen pressure, d is the distance between electrodes) and fixed reduced electric field strength $E/p = U_{bias}/(pd)$. The integral of the discharge current for different distances between the electrodes is presented in figure 4. The obtained plasma did not scale with pd parameter. It showed that dynamic effects were important in plasma generation.

IV.C. Axially symmetric plasma probe

To make a detailed investigation of plasma evolution the plasma probe diagnostic was used. The probe was installed on the symmetry axis of the chamber to allow direct simulations of the probe characteristics with the 2D plasma model.

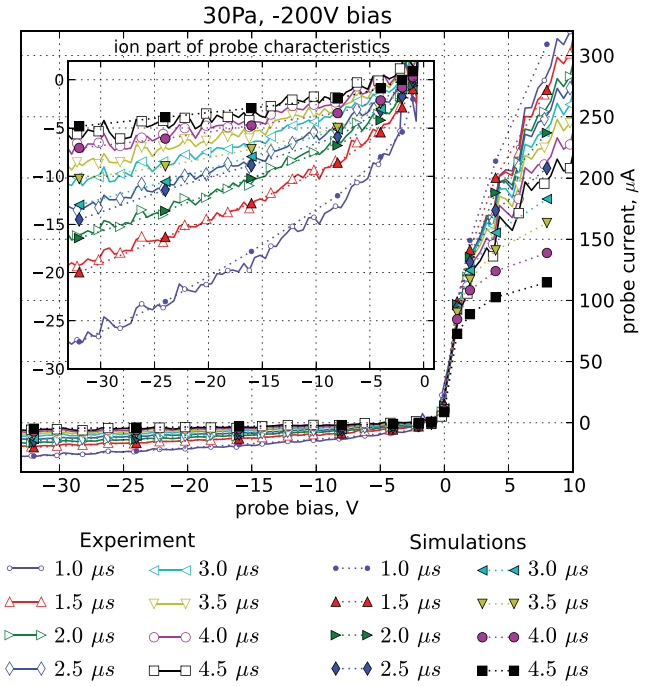

Figure 5. Comparison between simulated and measured probe characteristic for 30 Pa and −200 V bias. The ion part of the probe (scales: μA versus V) characteristic is shown in the inset.

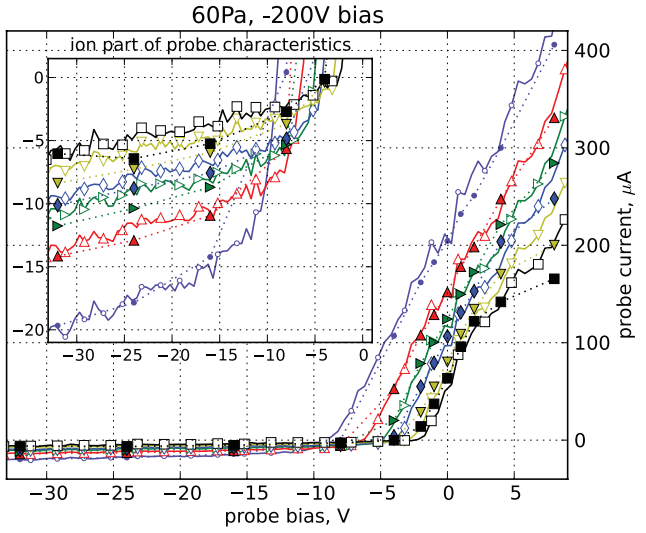

Figure 6. Comparison between simulated and measured probe characteristic for 60 Pa and −200 V bias. The ion part of probe (scales: μA versus V) characteristic is shown in the inset. The line legend is the same as in figure 5.

The probe measurements were performed at 30 Pa and 60 Pa hydrogen, the bias between the electrodes was −200 V in both cases. The simulated and measured probe characteristics were shifted by 1 V for 30 Pa and by 2 V for 60 Pa. This shift could have numerous causes, therefore, the measured probe characteristics were shifted by these values to the negative probe voltages. The measured probe characteristics and the comparison with the simulations are presented in figures 5 and 6. All presented simulations use the same initial input data apart from those varied in the experiments.

To take into account the characteristic response time of the SPU, the simulated probe response was numerically convoluted with $C \cdot \exp(-t/t_0)$, here $t_0 \sim 100$ ns is the SPU response time and constant C is chosen such that the collected charge is preserved during numerical integration.

The agreement between the simulated and measured probe characteristic is good up to 2.5 μs after the start of the UV pulse for the both pressures. At later times, the agreement is worse, due to the response of the simulated probe changing because the tip of the probe is no longer in the region containing a plasma (see figure 8). The transition of the probe from inside to outside the plasma (for the case of 30 Pa) occurs between 2.5 μs and 3.5 μs, however, the exact transition time is very sensitive to the model input parameters. After the transition (4.0–4.5 μs, 30 Pa, −200 V), the good agreement between the measured and modeled ion contribution to the probe characteristic is restored. Furthermore, despite the plasma no longer covering the entire probe, the probe response appears normal.

For the case of 60 Pa, −200 V (figure 6), the transition occurs later due to a larger contribution from collisions with the background gas. Therefore, the ion part of the probe characteristics for 4.5 μs for 60 Pa slightly deviates from the experimental one, while for 30 Pa the agreement is good.

The electron contribution to the simulated probe characteristics in figure 5 deviates significantly from the experiment occasionally from 2 μs onwards for a pressure of 30 Pa. But, at 60 Pa (figure 6), the deviation of the electron part is much smaller and only pronounced from 3.5 μs and for a probe bias larger than 5 V. These differences can be attributed to the combined effects of the uncertainties in electron–neutral cross-section set and some secondary effects (e.g. reflection of electrons from the aluminium surface), which are not taken into account. However, the simulations accurately reproduce the transition from the ion part to the electron part of the probe characteristic in both cases.

Interestingly, the apparent shift of the probe characteristic in figure 6 with time is reproduced by the model. Usually such a shift in the stationary plasma conditions may be explained by partial presence of the probe in or near the plasma sheath. However the reason of the shift in the case of a pulsed plasma may have other causes. As is seen in figure 7, the change of the sign of the probe current can not be explained by the presence of the probe in the sheath.

However, the shape of simulated plasma distortions depends on the dimensions on the probe. We simulated the plasma evolution with ten times thinner and two times shorter probe. We found that, although the distortion of the plasma around the probe was different, it was still significantly distorted. The shape of distortion was similar to described in [25].

Interestingly, for the ten times thinner probe the role of ion neutral collisions are expected to be of the same importance for the analysis of the probe response as for the used probe. The size of plasma sheath near the probe is determined by the the Debye length of the plasma. For the considered conditions, it can be estimated as $\lambda_D \sim 0.23$ mm (i.e. for $n_e \sim 5 \cdot 10^8 1$ cm^{-3} and $T_e \sim 0.5$ eV). Therefore, we do not expect the sheath size to decrease significantly for a probe with a radius of 0.025 mm as compared to 0.25 mm for the same probe biases. Hence, the number of the collisions in the probe sheath should be comparable in both situations.

Therefore, the application of a smaller probe in the considered discharge does not necessarily lead to negligible distortion nor to transition from collisional to collision less ion currents to the probe.

IV.D. Comparison between computed plasma density and that derived from measured probe characteristic

The 2D particle-in-cell simulations showed that probe diagnostics are not well suited to the considered plasma, because the plasma is spatially inhomogeneous along the probe length (see figure 8 with probe and figure 9 without probe). However, it is still interesting to apply probe theories to the measured probe characteristics, since in the general case, the distortion of the plasma by the probe is not known in advance. Furthermore, the probe response appears to be normal with distinct ion and electron parts, which would normally be used as evidence that probe theory can be applied.

We applied the Bernstein–Rabinowitz–Laframboise (BRL) [26], Allen–Boyd–Reynolds (ABR) [27, 28] and Talbot and Chou theory [29] modified by Tichý *et al* [30] (TCT) to analyze the probe I–V characteristics. We used the ESP_BRL and ESP_ABR programs [2] to obtain BRL and ABR fits for the probe characteristics. The fit results are presented in table 1. The electron temperature in the simulations after 1 μs was approximately 0.3 eV for 60 Pa and ~0.5 eV for 30 Pa. This corresponds to the estimate from the probe response, but the simulated EDF has a non-Maxwellian tail due to the presence of an external bias.

The most abundant ion in the considered conditions is H_3^+ [17]. The mobility of this ion in H_2 increases with increasing ion energy, due to a local minimum in the effective momentum transfer cross-section around 0.8 eV [17] in the center of mass reference frame. The energy range, where mobility changes significantly is smaller than the absolute value of the probe voltage. Modification of the probe theory to include variable collisional cross-sections is out of the scope of this paper, since this effect is included in the PIC model. Therefore, we performed the fitting procedure using the TCT theory with a collisional correction corresponding to the zero field mobility of H_3^+ in H_2, and for increased mobility, the corresponding reduced mobilities are ~11.3 cm^2 (V·s)$^{-1}$ and ~16 cm^2 (V·s)$^{-1}$. The resulting ion densities obtained are presented in the table 1.

It is also worth noting that an *a posteriori* estimate of the applicability of the probe method can lead one to incorrectly assume that a chosen probe theory is appropriate. Consider that, in the cylindrically symmetric setup here, the plasma density and radius can be estimated from the probe response via the BRL and TCT theories. The radial dimension of the plasma can be estimated to be $r \geqslant \sqrt{Q_c/(\pi q_e N_i d)} = 1.5$ cm, where $Q_i \sim 4$ nC (see figure 4), $d = 5$ cm is the distance between the electrodes, and N_i is the density estimate obtained from the chosen probe theory. Therefore, we conclude (incorrectly) that the ratio of radial plasma size to the Debye radius is, in this case, at least 75, based on an estimated plasma

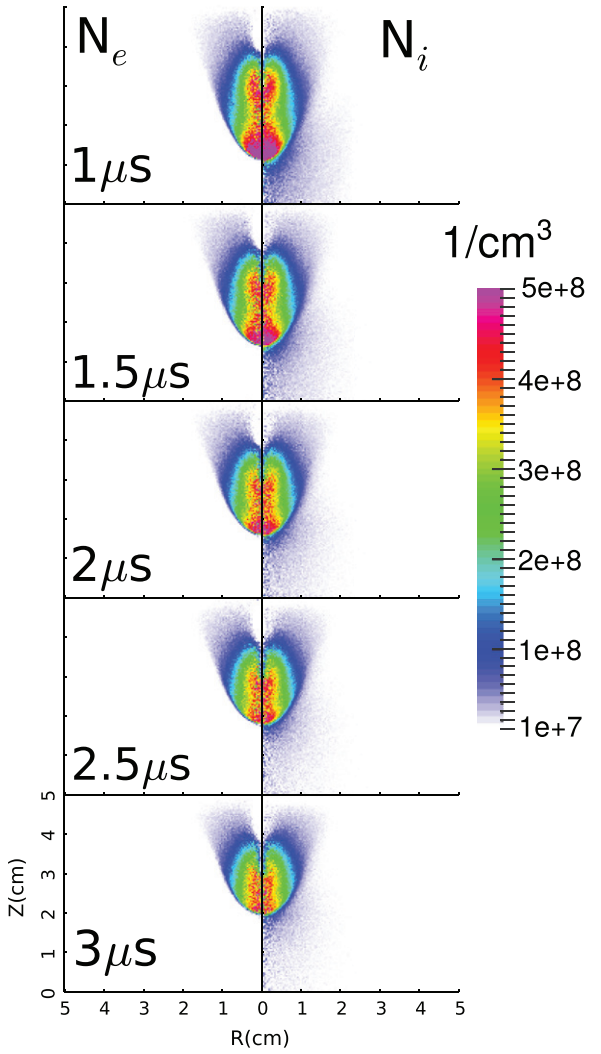

Figure 7. Electrons and ions (summed over ions types) densities for the different moments of time from the start of the UV pulse. Simulation for 60 Pa H_2, −200 V bias between electrodes and −4 V on the probe. The probe current for this condition changes sign from positive at 1.5 μs to negative at 3 μs, despite the plasma completely covering the probe.

density of $7 \times 10^8 1\ \mathrm{cm}^{-3}$ from probe theory. From the arguments above, it would be argued that the probe theory will provide reasonable estimates of the plasma density. However, this conclusion is wrong, since the simulations show that the plasma density varies significantly near the probe.

The differences between predictions of the different theories are large (see table 1). The BRL results correspond to the upper estimate of the plasma density, while ABR provides the lowest estimate for all probe biases. The results obtained with help of TCT theory tends to provide intermediate results. Similar trends are commonly reported elsewhere (for example in [31, 32]).

Nevertheless, as reported in [31–33], the plasma density tends to be between the results of BRL and ABR in many different experiments. Furthermore, the plasma density estimates from many collisional probe theories are also bounded by the density estimates of BRL and ABR. Hence, it is reasonable to take the difference between the density estimates of BRL and ABR as an approximation of the error margin of the probe measurements if the validity of the probe theory for the case of the plasma in question has not been validated by some independent numerical or experimental technique.

Table 1. Comparison of the ion density obtained from the simulations to the calculated with help of the different probe theories from the measured probe response.

						Simulation	
	Time[a] (μs)	T_e (eV)	BRL [26]	ABR [27, 28]	TCT[b] [30]	With probe[c]	No probe[d]
			Plasma density 10^8 cm^{-3}				
30 Pa	1	0.5	7.5	1.4	6.5–9	1–5	3–5
	2	0.3	5	0.6	3–5	1–5	2.5–4.5
	3	0.3	3	0.5	1.2–2	0.5–5	2–4.5
60 Pa	1	0.4	6	1	4–7	1–5	1–2.5
	2	0.3	3.5	0.4	1–2.5	1–5	1.5–2.5
	3	0.3	2	0.3	0.7–1.0	0.5–5	1.5–2.5

[a] Time is relative to the start of the UV pulse.
[b] The lower estimate of the ion density corresponds to the lower estimate of the reduced mobility of H_3^+ in H_2 (see text).
[c] The simulated plasma density near the probe significantly depends on the probe bias. The lower limit corresponds to the spatial minimum of the plasma density for a bias of −32 V on the probe, the upper limit corresponds to the spatial maximum plasma density for 0 V on the probe. Both minimum and maximum values are estimated in the quasi neutral region of the plasma.
[d] The plasma density is sampled over the region corresponding to probe position in experiments and simulations with probe.

The present study shows, that in spite of the plasma's significant spatial inhomogeneity, the probe can still have the expected response with distinct ion and electron parts. The simulations showed that, even when the probe tip is outside of the plasma, the probe response varies smoothly in time (see figure 8). These significant distortions can not be easily deduced from the probe response alone.

Therefore, an independent method for evaluating the applicability of the probe method should be used, e.g. optical emission spectroscopy. If independent diagnostics can not be applied, we recommend to estimate the uncertainty as the difference between the fit results of BRL and ABR.

V. Conclusions

In this paper, we have reported the results of a comparison between the predictions of a 2D PIC model, and experimental measurements of a low density transient plasma.

Our 2D PIC model of the plasma evolution takes into account the full geometry of the chamber. Therefore, it allows other experimental data, such as discharge characteristic measurements, to be used to verify assumptions about unknown and/or poorly known parameters, and to check the applicability of the model itself on the integral parameters before analysis of the complicated plasma probe characteristics.

Our results show good agreement between time resolved simulated and measured probe characteristics for two pressures with the same parameter set. This shows that the simulated plasma parameters, such as electron and ion densities, can be relied upon, because, in our simulations, the

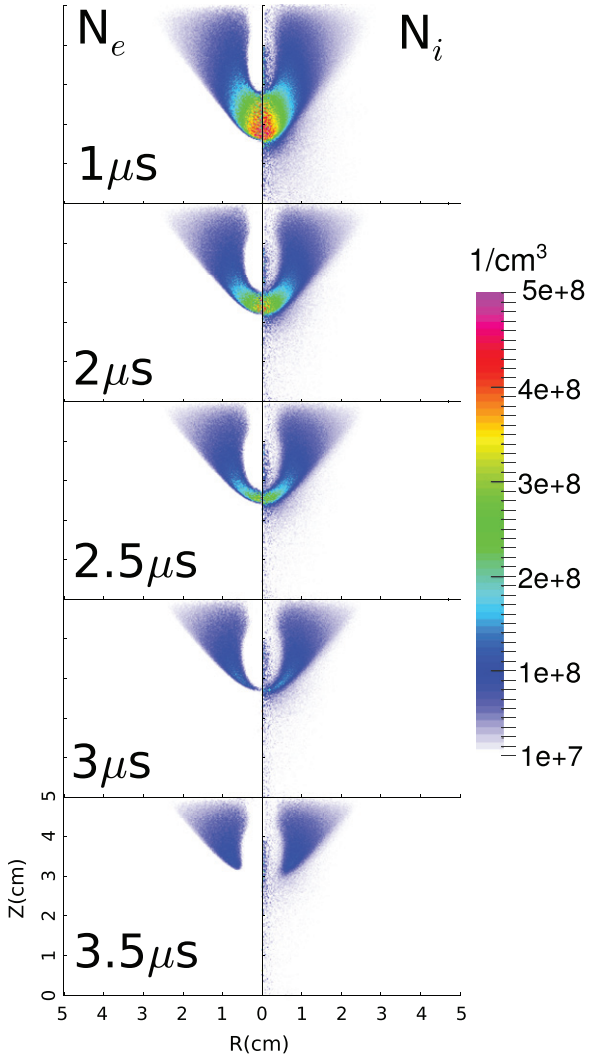

Figure 8. Electrons and ions (summed over ions types) densities for the different moments of time from UV pulse start. Simulation for 30 Pa H_2, −200 V bias between electrodes and −32 V on the probe.

probe was included as an electrode. Therefore, the interaction of the probe with the plasma is taken into account directly.

Our measurements also show that the measured probe characteristics have the proper shape with distinct ion and electron contributions, which would normally be taken as a sign that the parameters estimated from probe measurements would be accurate.

Nevertheless, probe theories, in the case of a low density non-stationary plasma, should be used with caution. Because, our simulation results demonstrate that, even in the case where the distortion of the plasma by the probe is obviously large (see figure 8), the probe response appears to be normal. Therefore, the application of the probe theory may yields misleading results, which in our case, is the overestimation of the plasma density by a factor of three to seven along the surface of the probe for the BRL and TCT theories and significant underestimation of the maximum plasma density by the ABR theory.

Hence, in the general case, the application of probe theory cannot be justified by probe measurements alone, and an other method should be used to verify the results of the probe method. If independent diagnostics can not be applied, we recommend to estimate the uncertainty as the difference between the fit results of BRL and ABR theories.

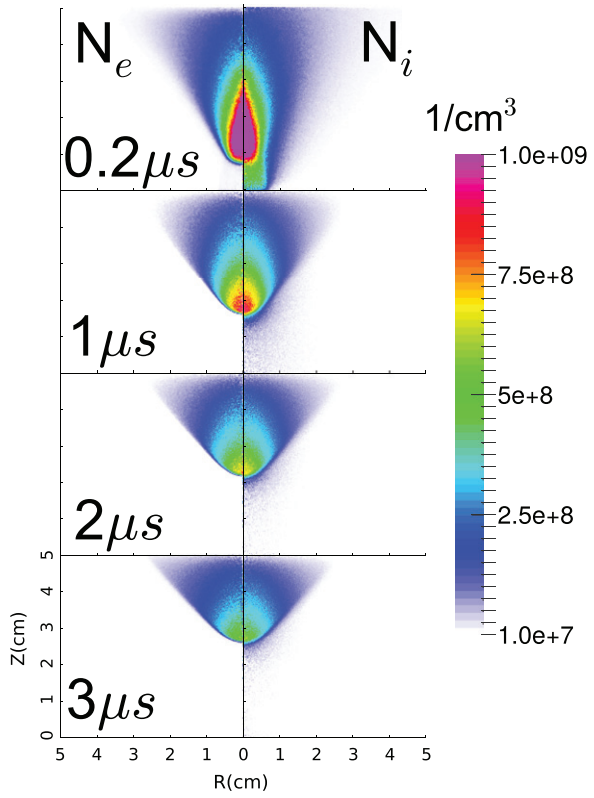

Figure 9. Electrons and ions (summed over ions types) densities for the different moments of time from UV pulse start. Simulation for 30 Pa H_2, −200 V bias between electrodes without probe in the chamber.

Acknowledgments

The authors would like to thank T Rakhimova for helpful discussion. This work is part of the research program 'Controlling photon and plasma induced processes at EUV optical surfaces (CP3E)' of the 'Stichting voor Fundamenteel Onderzoek der Materie (FOM)' which is financially supported by the Nederlandse Organisatie voor Wetenschappelijk Onderzoek (NWO). The CP3E programme is cofinanced by Carl Zeiss SMT GmbH (Oberkochen), ASML (Veldhoven), and the AgentschapNL through the Catrene EXEPT program.

References

[1] Hutchinson I H 2005 *Principles of Plasma Diagnostics* (Cambridge: Cambridge University Press)
[2] Chen F F 2003 Langmuir probe diagnostics *Mini-Course on Plasma Diagnostics, IEEE-ICOPS Meeting* (*Jeju, Korea, 2003*)
[3] Birdsall C K and Bruce Langdon A 1985 *Plasma Physics via Computer Simulation* (New York: McGraw-Hill)
[4] Raizer Yu P 1991 *Gas Discharge Physics* (Berlin: Springer)

[5] Lide D R 2003 *CRC Handbook of Chemistry and Physics 2003–2004: a Ready-Reference Book of Chemical and Physical Data* (Boca Raton, FL: CRC)
[6] Lakits G, Aumayr F, Heim M and Winter H 1990 Threshold of ion-induced kinetic electron emission from a clean metal surface *Phys. Rev.* A **42** 5780
[7] Winter H, Aumayr F and Lakits G 1991 Recent advances in understanding particle-induced electron emission from metal surfaces *Nucl. Instrum. Methods Phys. Res.* B **58** 301–8
[8] Kishinevsky L M 1973 Estimation of electron potential emission yield dependence on metal and ion parameters *Radiat. Eff.* **19** 23–7
[9] Agarwala V and Fort T 1974 Work function changes during low pressure oxidation of aluminum at room temperature *Surf. Sci.* **45** 470–82
[10] Sosa E D 2002 The electron emission characteristics of aluminum, molybdenum, carbon nanotubes studied by field emission and photoemission *PhD Thesis* University of North Texas
[11] Helm H 1988 Measurement of the ionization potential of triatomic hydrogen *Phys. Rev.* A **38** 3425–9
[12] Winter H, Eder H, Aumayr F, Lorincik J and Sroubek Z 2001 Slow-ion induced electron emission from clean metal surfaces: 'subthreshold kinetic emission' and 'potential excitation of plasmons' *Nucl. Instrum. Methods Phys. Res.* B **182** 15–22
[13] Bogaerts A and Gijbels R 2002 Hybrid monte carlo—fluid modeling network for an argon/hydrogen direct current glow discharge *Spectrochim. Acta* B **57** 1071–99
[14] Baragiola R A, Alonso E V and Oliva Florio A 1979 Electron emission from clean metal surfaces induced by low-energy light ions *Phys. Rev.* B **19** 121
[15] Langmuir I 1923 The effect of space charge and initial velocities on the potential distribution and thermionic current between parallel plane electrodes *Phys. Rev.* **21** 419–35
[16] Phelps A V 1990 Cross sections and swarm coefficients for H^+, H_2^+, H_3^+, H, H_2, and H^- in H_2 for energies from 0.1 eV to 10 keV *J. Phys. Chem. Ref. Data* **19** 653
[17] Šimko T, Martišovitš V, Bretagne J and Gousset G 1997 Computer simulations of H^+ and H_3^+ transport parameters in hydrogen drift tubes *Phys. Rev.* E **56** 5908–19
[18] Mokrov M S and Raizer Yu P 2008 Monte carlo method for finding the ionization and secondary emission coefficients and I–V characteristic of a townsend discharge in hydrogen *Tech. Phys.* **53** 436–44
[19] Nanbu K 1994 Simple method to determine collisional event in monte carlo simulation of electron-molecule collision *Japan. J. Appl. Phys.* **33** 4752–3
[20] Skullerud H R 1968 The stochastic computer simulation of ion motion in a gas subjected to a constant electric field *J. Phys. D: Appl. Phys.* **1** 1567
[21] Yoon J-S, Song M-Y, Han J-M, Hwang S H, Chang W-S, Lee B-J and Itikawa Y 2008 Cross sections for electron collisions with hydrogen molecules *J. Phys. Chem. Ref. Data* **37** 913
[22] Ehrhardt H, Langhans L, Linder F and Taylor H S 1968 Resonance scattering of slow electrons from H_2 and CO angular distributions *Phys. Rev.* **173** 222
[23] Dutton J 1975 A survey of electron swarm data *J. Phys. Chem. Ref. Data* **4** 577–856
[24] Graham E, James D R, Keever W C, Albritton D L and McDaniel E W 1973 Mobilities and longitudinal diffusion coefficients of mass-identified hydrogen ions in H_2 and deuterium ions in D_2 gas *J. Chem. Phys.* **59** 3477–81
[25] Taccogna F, Longo S and Capitelli M 2008 Ion-neutral collision effects in langmuir probe theory *Contrib. Plasma Phys.* **48** 509–14
[26] Laframboise J G 1966 Theory of spherical, cylindrical langmuir probes in a collisionless, maxwellian plasma at rest *Technical Report UTIAS Report* NO. 100 DTIC Document University of Toronto and Institute for Aerospace studies
[27] Allen J E, Boyd R L F and Reynolds P 1957 The collection of positive ions by a probe immersed in a plasma *Proc. Phys. Soc.* B **70** 297–304
[28] Chen F F 1965 Numerical computations for ion probe characteristics in a collisionless plasma *J. Nucl. Energy* C **7** 47–67
[29] Talbot L and Chou Y S 1969 Langmuir probe response in the transition regime *Rarefied Gas Dyn.* **2** 1723–37
[30] Tichý M, Š M, David P and David T 1994 A collisional model of the positive ion collection by a cylindrical langmuir probe *Contrib. Plasma Phys.* **34** 59–68
[31] Chudáček O, Kudrna P, Glos J, Š M and Tichý M 1995 Langmuir probe determination of charged particle number density in a flowing afterglow plasma *Contrib. Plasma Phys.* **35** 503–16
[32] Iza F and Lee J K 2006 Particle-in-cell simulations of planar and cylindrical langmuir probes: Floating potential and ion saturation current *J. Vac. Sci. Technol.* A **24** 1366–72
[33] D-Cabrera J M, Ballesteros J, Fernández J I and Tejero-del A 2015 Experimental radial motion to orbital motion transition in cylindrical langmuir probes in low pressure plasmas *Plasma Sources Sci. Technol.* **24** 025026